Strengthening in TiB Reinforced Dual-phase Titanium Matrix Composites: Effect of TiB Volume Fraction and Matrix Microstructure

Zheyu Miao[a,b,1], Yu chen[a,1], Qiang Li[b,*], Yakai Zhao[c,d], Kai Chen[a,*], Yimin Gao[a], Upadrasta Ramamurty[b]

[a] State Key Laboratory for Mechanical Behavior of Materials, School of Materials Science and Engineering, Xi'an Jiaotong University, Xi'an, Shaanxi 710049, PR China

[b] School of Mechanical and Aerospace Engineering, Nanyang Technological University, Singapore 639798, Republic of Singapore

[c] Future Energy Acceleration & Translation (FEAT), Agency for Science, Technology and Research (A*STAR), Singapore 138634, Republic of Singapore

[d] Institute of Materials Research and Engineering (IMRE), Agency for Science, Technology and Research (A*STAR), Singapore 138634, Republic of Singapore

[1] Zheyu Miao and Yu Chen contributed equally to this work.

[*] Corresponding author: liqiangmse@gmail.com (Qiang Li); kchenlbl@gmail.com (Kai Chen)

Abstract

The influence of matrix microstructure on the strengthening behavior of titanium matrix composites (TMCs) has been rarely explored, and existing strengthening models often overlook the complexity introduced by dual-phase microstructural evolution. In this study, a series of TiB-reinforced dual-phase TMCs containing 0–8 vol.% TiB were fabricated via powder metallurgy (PM) and then heat treated following different protocols, resulting in equiaxed, lamellar, bimodal, and basketweave matrix microstructures. The effects of TiB content and matrix microstructure on mechanical properties and strengthening mechanisms were systematically examined through uniaxial compression and hardness tests. A schematic continuous cooling transformation (CCT) diagram was constructed to correlate phase evolution with processing conditions. Quantitative analysis of the

strengthening mechanisms reveal that load-transfer is the dominant contributor. When the matrix morphology and hardness remain invariant, a constant strengthening efficiency of ~40 MPa per vol.% TiB was observed. However, variations in the proportion of hard phases (e.g., β_{tf} and α') in matrix significantly affect the strengthening efficiency. These findings highlight the pivotal role of matrix microstructure in governing the mechanical behavior of dual-phase TMCs and provide insights for more accurate modeling and design of advanced composites.

Keywords:

Metal matrix composites, Titanium alloys, Powder metallurgy, Strengthening mechanism, Phase transformation

I. INTRODUCTION

Titanium and its alloys are widely used in the aerospace, chemical, marine, and biomedical industries owing to their outstanding mechanical and physical properties, including high specific stiffness and strength at both ambient and elevated temperatures, along with excellent corrosion and oxidation resistances [1]. To further enhance their specific strength and service temperature, titanium matrix composites (TMCs) with various ceramic reinforcements are being explored [2-4]. Amongst them, TMCs with TiB (and TiC) are the most widely studied [3]. TiB is particularly attractive due to its high elastic modulus (~450–550 GPa) [3, 5], high melting point (~2200 °C) [6], and excellent compatibility with the titanium matrix. The closely matched thermal expansion coefficients (CTE; $CTE_{Ti} = 9 \times 10^{-6}$ K^{-1} and $CTE_{TiB} = 8.6 \times 10^{-6}$ K^{-1} [7]), nearly identical densities ($\rho_{Ti} = 4.57$ g/cm^3 and $\rho_{TiB} = 4.56$ g/cm^3 [6]), and low lattice mismatch (<3.6% [8, 9]) ensure good interfacial coherence, making TiB an ideal reinforcement candidate.

Various strategies have been developed to strengthen TMCs, which generally fall into two categories, i.e., tailoring either the reinforcement characteristics or matrix microstructure. On the reinforcement side, considerable efforts have been made on increasing the TiB volume fraction [10, 11] and aspect ratio [11, 12], reducing the particle size to the nanoscale [13], and tailoring their spatial distribution [14-16]. Increasing the volume fraction of TiB (vol.% TiB) enhances yield strength (σ_y) at the cost of ductility. For instance, with a 6.8 vol.% TiB reinforcement Ti6Al4V achieved a σ_y of 1110 MPa, an increment of 29.8% over unreinforced Ti6Al4V [10], although further increases in vol.% TiB led to premature fracture and strength reduction. Increasing the aspect ratio of TiB is also effective [11, 12]. A TiB/Ti6Al4V composite nanowire with 5 vol.% TiB (aspect ratio ~300) reached a σ_y of 1163 ± 13 MPa, 23.2% higher than unreinforced nanowires [17]. Particle size refinement through rapid solidification techniques, such as additive manufacturing or spark plasma sintering, has further pushed σ_y to ~1200 MPa [18]. While tailoring TiB distribution can help

improve the strength-ductility-toughness synergy [14, 15, 19, 20], these strategies alone generally yield modest strength improvements. Another approach involves hybrid reinforcement, incorporating silicide [21, 22], carbide [23], or oxide [24]. For example, a (4 vol.% Ti_5Si_3 + 3.4 vol.% TiB)/ Ti6Al4V composite showed σ_y of 1050 ± 9 MPa (with 5% elongation), 12.9% higher than the counterpart without silicide [25].

In contrast to reinforcement-focused strategies, the influence of the matrix on TMC performance has received relatively less attention. Heat treatment has been demonstrated to be highly effective. For example, a 5 vol.% TiB/Ti6Al4V composite reached a peak σ_y of 1334 MPa (with 6.1 % elongation) after solution and aging treatments [26]. Using stronger matrix alloys also improves the strength of TMCs [22, 27, 28]. A 3.5 vol.% TiB-reinforced TA15 (a near-α-Ti alloy with nominal composition Ti-6Al-2Zr-1Mo-1V) showed slightly higher strength than a 5 vol.% TiB/Ti6Al4V composite [28]. Thermomechanical processing has also been explored to optimize both matrix microstructure and TiB alignment [29-31]. For example, (TiB + TiC + La_2O_3)/IMI834 composites reached a σ_y of 1267 MPa (albeit with negligible ductility) after forging and heat treatment [32]. Another Ti6Al4V based composite with 1.55 wt.% B attained a σ_y of 1380 MPa (elongation of 4.6%) after rolling, forging and heat treatment [33]. However, despite its effectiveness in strengthening, thermomechanical processing is limited by potential issues, including reinforcement fragmentation and the introduction of significant anisotropy during deformation [34-36].

Most strengthening mechanisms reported in TMCs, such as the particle strengthening through the Orowan looping mechanism and load-transfer strengthening, were originally developed based on studies of Al- or Mg-matrix composites [16, 37, 38]. The matrices in Al- and Mg-based composites are typically single-phase (i.e., α-Al or α-Mg), lacking the allotropic α/β transformations that is a distinct characteristic of Ti alloys. This raises the question of whether those conventional models can be directly applied to TMCs, which commonly possess more complex

dual-phase (α/β) microstructure. According to the morphology of α phase, the microstructure of dual-phase Ti alloys (TA15 in this work) can be categorized into equiaxed, lamellar, bimodal, and basketweave types [39-42]. The equiaxed microstructure refers to the as-sintered state of the TiB/TA15 composite, in which near-equiaxed or globular α is surrounded by the β ligaments. The lamellar structure, commonly observed in as-cast and as-sintered TA15, consists of alternating α and β lamellae that form a colony with a common crystallographic orientation, distinct from that of adjacent colonies. The bimodal microstructure comprises primary α (α_p) and transformed β structure (β_{tf}, consisting of secondary acicular α′ and retained β matrix), obtained through solution treatment below T_β. The basketweave structure is generated by solution treatment above T_β, which induces rapid allotropic transformation of β to fine acicular α′ with multiple orientations within a single prior β grain.

In our prior investigation on the TiB-reinforced dual phase TMCs fabricated using the powder metallurgy technique [19], even 1 vol.% TiB addition induced a noticeable shift of matrix microstructure from a Widmanstätten structure (with α/β lamellae and α_{GB}) to a nearly equiaxed morphology. This transition significantly affected the strength, ductility, and fracture toughness of the composites. For example, the unreinforced dual-phase Ti alloy with the Widmanstätten structure and α_{GB} exhibited approximately three times higher fracture toughness than the 1 vol.% TiB/TMC, despite the latter exhibiting higher strength and ductility. The superior fracture toughness of the unreinforced alloy was attributed to the effective deflection of cracks via premature decohesion along α_{GB}, a toughening mechanism largely absent in TMCs.

In light of the above considerations, a series of TA15 matrix composites reinforced with varying TiB contents (0–8 vol.%) were fabricated via powder metallurgy route using aluminum diboride (AlB_2) as the boron precursor. A variety of heat treatment protocols were employed to tailor the matrix microstructures, resulting in lamellar, bimodal, and basketweave structures. The strengthening mechanisms in

TiB/TA15 composites with different matrix microstructures were systematically investigated through uniaxial compression and hardness tests. Additionally, phase evolution in these TMCs were elucidated and summarized in a schematic continuous cooling transformation (CCT) diagram.

II. MATERIALS AND METHODS

The raw materials used for fabricating TiB/TA15 composites included fine AlB_2 (<5 μm) powder and spherical gas atomized TA15 (near α-type Ti alloy, Ti-6.5Al-2Zr-2V-1.5Mo, ~100 μm) powder [19]. Composites with varying TiB volume fractions, V_{TiB}%, of 0%, 1%, 2%, 4%, 6%, and 8% were fabricated by ball milling and hot-press sintering processes [19, 20]. First, AlB_2 and TA15 powders were mixed in predefined proportions and subjected to planetary ball milling in a stainless-steel jar with agate milling balls under an argon atmosphere. The rotational speed, milling time and ball-to-powder ratio employed for each batch were 150 rpm, 8 h, and 5:1, respectively. The primary purpose of the ball milling process is to uniformly coat the large TA15 particles with tiny AlB_2 satellite particles. Then, the mixed powders were put into columniform graphite molds (diameter of 45 mm) and consolidated via reaction sintering using a vacuum hot-press system (10^{-3} Pa). The powders were first preheated to 250 °C and held for 30 minutes to remove residual moisture and gas. Subsequently, sintering was performed at 1200 °C under 20 MPa for 60 minutes, followed by furnace cooling in vacuum. During this process, the in-situ reaction between AlB_2 and Ti (AlB_2 +2Ti → 2TiB +Al) facilitated the formation of TiB, as documented in Refs.[11, 19, 20]. The resulting samples were cylindrical, measuring 45 mm in diameter and 8 mm in height. The as-sintered samples are designated as S0–S8 according to the corresponding vol.% TiB. The oxygen, nitrogen, and hydrogen contents were measured by inert gas fusion (ONH836), and the concentration of other alloying elements were evaluated using inductively coupled plasma optical emission spectroscopy (ICP-OES, Agilent 5110). Both the starting pre-alloyed TA15 powder and the as-sintered TMCs exhibited

extra-low interstitial (ELI) levels, with <0.001 wt% N, <0.01 wt% H, and <0.01 wt% O. The detailed chemical compositions of TiB/TA15 composites are listed in **Table S-I** in the Electronic Supplementary Materials.

The beta-transus temperature (T_β, the temperature at which $\beta \leftrightarrow \alpha + \beta$ transformation occurs) for TiB/TA15 composites was estimated using empirical Equation (1) [43, 44]:

$$T_\beta = T_0 + 21.1\,[Al] + 4.2[Sn] + 23.3[Si] + 123.0[O] \\ -9.5[Mo] - 6.9[Zr] - 11.8[V] - 12.1[Cr] - 15.4[Fe] \#(1)$$

where [M] is the weight fraction of the alloying element M, and T_0 is the beta-transus temperature of base alloy. Based on literature data [45-48], T_β of the base TA15 alloy ranges ~990–1030 ^{o}C. The AlB_2 addition introduced various content of Al (up to ~1.7wt% in S8), a strong α-stabilizer that increases T_β by an estimated 5 ^{o}C for S1 and 36 ^{o}C for S8. Consequently, the T_β of these TMCs was estimated to fall within ~995–1066 °C. Accordingly, three solution temperatures were selected: 950 ^{o}C (α+β region), 1050 ^{o}C (near T_β), and 1150 ^{o}C (β region). All solution treatments lasted 40 minutes and was followed by water quenching. The solution treated samples are renamed as STX_y, where ST denotes 'solution treatment', X represents the TiB volume fraction, and y represents the ST temperature.

Subsequent to ST, aging treatments were applied to part of the samples subjected to 1150 ^{o}C solution treatment, in which the matrix microstructure has fully transformed into martensite. The martensitic decomposition temperature (T_{dec}, $\alpha' \rightarrow \alpha + \beta$) of TA15 is above 600 ℃ [28, 44, 49, 50] and significant α-lath coarsening occurs at 800 ℃ [51]. Keeping this in view, two representative aging temperatures, 500 and 700 ℃, were selected for comparison, each held for 5 h followed by air cooling. These samples are denoted as STAX_y, where STA for solution treatment and aging, X for TiB volume fraction, and y for aging temperature.

The microstructure was observed using optical microscopy (OM, LEICA DMI 5000 M) and scanning electron microscopy (SEM, TM3000 and JOEL7600) after the samples were fine polished and etched with the Kroll's reagent (5 vol.% HF + 10 vol.%

HNO_3 + 85 vol.% H_2O) [19]. Transmission electron microscopy (TEM, JEM-2100) was employed to identify various microstructural phases in TMCs. Electron backscattering diffraction (EBSD) mapping was carried out with a maximum step size of 0.5 μm over an area of ~0.3 mm^2. The EBSD data were analyzed using the AZTEC CRYSTAL software to determine grain orientations, boundaries, and sizes, and to reconstruct prior β grains based on the Burgers' orientation relationship of $(110)_{\beta\text{-Ti}}$ // $(0002)_{\alpha\text{-Ti}}$ and $<1\bar{1}1>_{\beta\text{-Ti}}$ // $<11\bar{2}0>_{\alpha\text{-Ti}}$ [1, 52]. Microstructural parameters, including area fraction of phases/microstructures, as well as minimum Feret's diameter and aspect ratio of TiB, were quantified using the Trainable Weka Segmentation plugin built in Fiji software from SEM-BSE images (representative examples are shown in **Figures. S-1 and S-2** in the Electronic Supplementary Materials) [53], with a total analyzed area of ~0.6 mm^2 per sample.

Room temperature compression tests were conducted on cylindrical specimens that are 5 mm in diameter and 13 mm in height using a universal testing machine (CMT 5305) at a constant crosshead speed of 6×10^{-4} s^{-1}. At least three samples were tested for each condition. Vickers hardness tests were performed using a digital microhardness tester (HXD-1000TMC) under 50gf (0.4903 N) load and 10 s dwell time, with minimum 15 indents per sample. Rockwell hardness tests were carried out using an automated tester (SHR-145N) with load of 60kgf (588.4 N) and dwell time of 10 s. At least 10 valid measurements were obtained for each sample.

III. RESULTS

A. *Microstructure of as-sintered TiB/TA15 composites*

X-ray diffraction (XRD) patterns obtained on the as-sintered TiB/TA15 composites are shown in **Figure S3**. They indicate the microstructural presence of α-Ti (hexagonal close-packed, hcp), β-Ti (body-centered cubic, bcc), and TiB (orthorhombic) phases, consistent with the results of prior investigations [19, 20]. An enlarged view of the [101] peak shows the shifting and sharpening of diffraction peak in α-Ti as shown in **Figure S3**(b), which is attributed to the increased Al concentration

in α-Ti and increased α-Ti lath width [54, 55].

Representative backscattered electron (BSE) images and EBSD maps of the as-sintered S0–S8 are shown in **Figure 1**, illustrating the microstructure evolution with increasing AlB_2 addition. Unlike the Widmanstätten structure (with α/β lamellae and colonies) commonly observed in the TA15 alloy (**Figures 1a$_1$, 1b$_1$–1b$_4$**) [19], the presence of TiB in S1–S8 leads to globular or near-equiaxed morphology, with the absence of (otherwise obvious) grain boundary α (α_{GB}) (**Figures 1a$_2$–1a$_4$**) [7]. While further investigations such as *in situ* experiments might be needed, this microstructural transition is generally attributed to the heterogenous nucleation of α-Ti on the TiB particles during the solid-state $\beta \rightarrow \alpha + \beta$ transformation upon slow cooling from temperatures above β-transus [7, 56]. Owing to their semi-coherent interfaces with α-Ti along specific crystallographic planes, TiB particles act as potent nucleation sites, promoting the direct formation of equiaxed α-Ti grains [8, 56-58]. Additionally, the TMCs in this work experience plastic deformation during hot-pressing sintering, which may further facilitate recrystallization during subsequent furnace cooling and the development of equiaxed α. In contrast, TiB particles exhibit a similar 'necklace' like distribution among S1–S8 samples (**Figures 1a$_2$–1a$_4$, 1c$_1$–1c$_4$**), while showing increased densification with increasing TiB content, consistent with prior reports on cast and PM TMCs [59-61]. This 'necklace' structure originates from the in-situ reaction between AlB_2 and Ti on the surface of spherical Ti powders, where AlB_2 particles were initially coated [11, 19]. Consequently, the TiB network sizes closely match those of the raw Ti powders, and the TiB spacing decreases with increasing AlB_2 volume fraction [11]. As demonstrated in previous studies [19, 20], the particles' location and characteristic microstructure size, such as colony size (μ_D) and prior β grain size (d_β), play crucial roles in affecting the mechanical behaviors of TMCs. In view of this, EBSD analysis was conducted. Significant reductions in both μ_D (from ~355.5 μm in S0 to ~41 μm in S1) and d_β (from ~782.2 μm in S0 to ~82 μm in S1) were observed with minor TiB addition, whereas both only show marginal

decrease with further TiB addition, reaching μ_D ~26 μm and d_β ~41 μm in S8 (**Figure 2a**). The observed microstructural refinement (i.e., reduction in μ_D and d_β) is attributed to the ability of TiB to pin prior β grain boundaries (Zener pinning effect) at elevated temperature and to heterogeneously nucleate α-Ti during cooling [58, 62]. The limited grain size reduction with further TiB addition is consistent to previous reports [56, 58, 63], and is likely due to the formation of the TiB 'necklace' formation that saturates the available heterogeneous nucleation sites. The area fractions of each phase are estimated using the BSE-SEM images and are summarized in **Figure 2b**. The area fraction of α-Ti increases with AlB_2 content, primarily because Al, an α-stabilizer, increases T_β and stabilizes α [52].

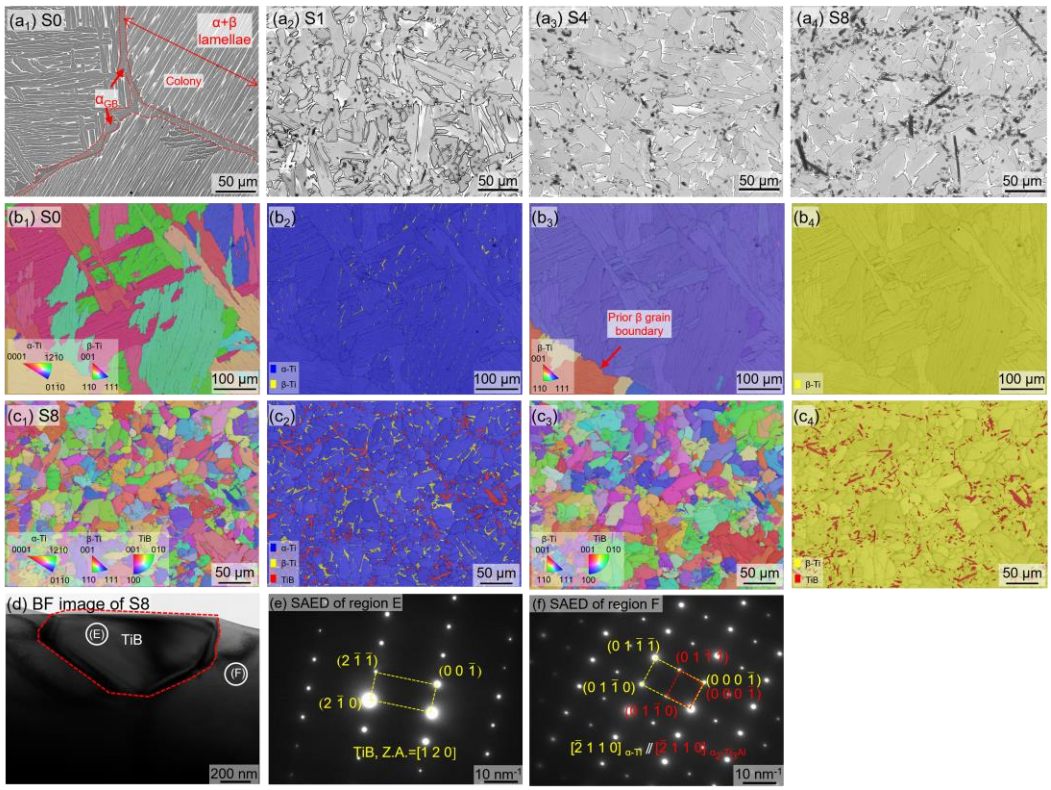


Figure 1. Representative microstructures of as-sintered TiB/TA15 composites: (a_1–a_4) BSE images of S0, S1, S4, and S8; (b_1–b_4) EBSD analysis of S0; (c_1–c_4) EBSD analysis of S8; (c, d, e) bright-field TEM image and corresponding SAED of S8 illustrating the presence of α_2-Ti_3Al. (b_1 and c_1) grain orientation map with IPF coloring, (b_2 and c_2) phase map, (b_3 and c_3) reconstructed prior β grain orientation map, and (b_4 and c_4) reconstructed phase maps.

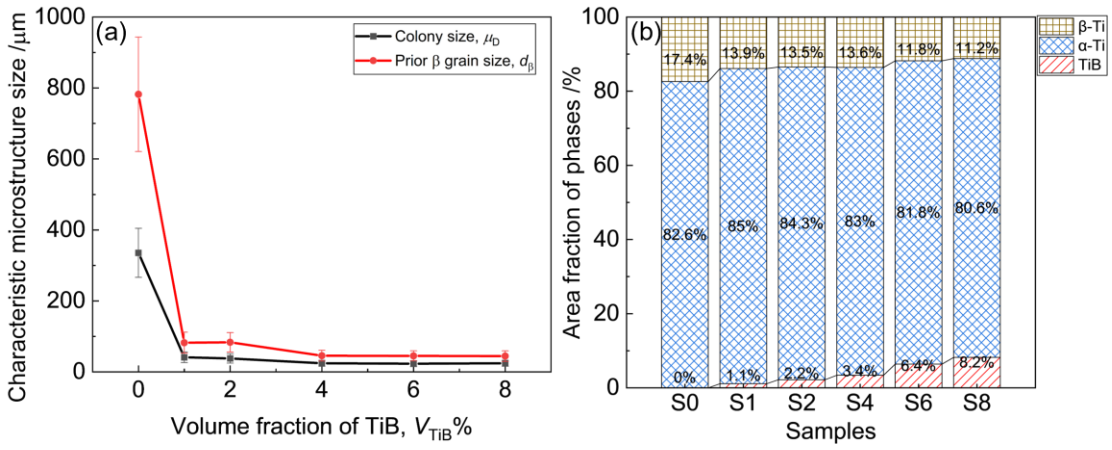


Figure 2. (a) Colony and prior β grain size, and (b) volume fractions of each phase in S0–S8.

The precipitation of the α_2-Ti_3Al phase (~1–2 nm [64]), an intermetallic compound with an hcp $D0_{19}$ structure that typically strengthens the alloy while simultaneously embrittling it, is commonly reported in near-α-Ti alloys when the solubility limit of Al (~7 wt.%) is exceeded [30, 45, 65]. While the presence of α_2-Ti_3Al was previously confirmed in the S4 sample [19], the present TEM analysis focuses on the S8 sample to examine the effect of further increased AlB_2 content. As shown in **Figures 1d, 1e, and 1f**, the selected area electron diffraction (SAED) pattern confirms the presence of α_2-Ti_3Al, which is an ordered superlattice structure formed within the α-Ti matrix. These precipitates exhibit a coherent interface and crystallographic orientation relationship with the α-Ti matrix: $[\bar{2}\,110]_{\alpha\text{-Ti}}$ // $[\bar{2}110]_{\alpha2\text{-Ti3Al}}$, $(000\bar{1})_{\alpha\text{-Ti}}$ // $(000\bar{1})_{\alpha2\text{-Ti3Al}}$, $(01\bar{1}0)_{\alpha\text{-Ti}}$ // $(02\bar{2}0)_{\alpha2\text{-Ti3Al}}$, and $(01\bar{1}\bar{1})$ // $(02\bar{2}\bar{1})$, consistent to previous reports [64, 65].

B. *Microstructure of solution treated TiB/TA15 composites*

As detailed in Section II, the estimated T_β for S0–S8 range from 990 to 1066 °C, with higher AlB_2 addition resulting in higher T_β. Based on this, three solution treatment temperatures were selected in this study: (1) 950 °C, representing the (α+β) two-phase region, below T_β, (2) 1050 °C, near the T_β, and (3) 1150 °C, corresponding to the β single-phase region, above T_β. Optical microscopy (OM) images of S0–S8 after solution treatment are displayed in **Figure S4**, and the corresponding backscattered

electron (BSE) images are illustrated in **Figure 3**. The volume fractions of matrix phases in these samples are measured using the SEM-BSE images and demonstrated in **Figure 4**.

As shown in **Figure 3**, the matrix microstructure of all the TiB/TA15 composites subjected to the ST_{950} treatment are composed of transformed β (β_{tf}) and primary α-Ti (α_p). Solution treated in the two-phase region ($M_s < T < T_\beta$), i.e, 950 °C in this work, the β phase is sufficiently stabilized and the martensitic transformation occurs upon water quenching, resulting in the appearance of β_{tf}. Compared to the β-Ti in as-sintered samples, the β_{tf} contains higher content of α-stabilizers (i.e., Al) and neutral elements (i.e., Zr), and lower Mo_{eq}, since part of α-Ti dissolves into β during the solution treatment (**Table I**). The volume fraction of β_{tf}, which progressively increases from 39% in $ST0_{950}$ to 55% in $ST8_{950}$ (**Figure 4a**), is significantly higher than the 24%–27% β-Ti content in as-sintered samples (**Figure 2b**), further supporting that some primary α-Ti (α_p) transforms to β-Ti during the solution treatment.

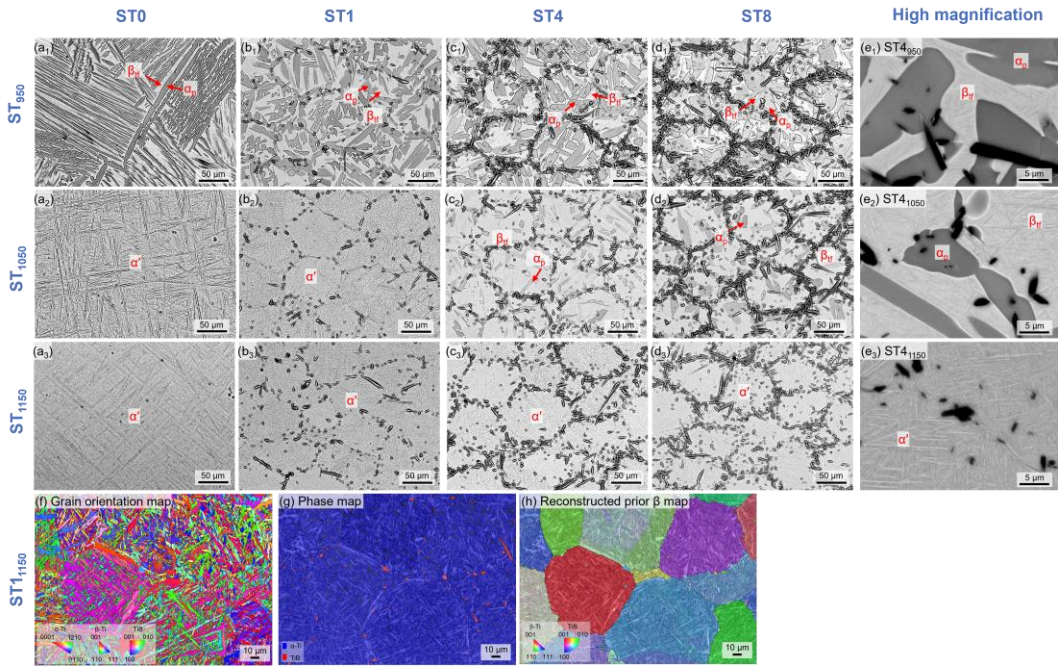


Figure 3. Representative microstructure of solution-treated TiB/TA15 composites at (a_1 – e_1) 950 °C, (a_2 – e_2) 1050 °C, and (a_3 – e_3) 1150 °C. The dark grey and light grey phases are α_p and β_{tf}, respectively. (f, g, h) representative EBSD analysis of $ST1_{1150}$ sample.

Table I. Chemical composition of β-Ti in S1 and β_{tf} in $ST1_{950}$ measured by EDS.

Samples	Phases	Chemical compositions (wt.%)				
		Al	Mo	V	Zr	Ti
S1	β-Ti	2.78	9.56	5.91	1.53	Bal.
$ST1_{950}$	β_{tf}	5.46	1.58	1.79	2.40	Bal.

Figures ($3a_2$ – $3e_2$) show the BSE-SEM images of the TiB/TA15 composites after solution treatment at 1050 ℃. The $ST0_{1050}$ and $ST1_{1050}$ samples exhibit fully needle-like α′ martensite, with no observable β_{tf} or α_p phases. In contrast, other samples still exhibit both β_{tf} and α_p microstructure. This difference arises from the higher Al (α-stabilizer) content introduced by the higher AlB_2 addition, which raises T_β. Additionally, and compared to ST_{950} treated series, the ST_{1050} treated series show a significant reduction in the α_p content (**Figures 4a and 4b**), indicating that more α_p transforms into β_{tf} at higher solution temperature.

Figures ($3a_3$ – $3e_3$) show the BSE-SEM images of TiB/TA15 composites after solution treatment at 1150 ℃, and representative EBSD maps obtained on the $STA1_{1150}$ sample are presented in **Figures (3f – 3h)**. The matrix microstructures of all composites have fully transformed into basketweave structure composed of acicular α′ martensite (**Figure 4c**), with an average width of ~4.8 ± 1.3 μm (which is the characteristic microstructure size for basketweave microstructure [66, 67]). The prior β grain size is estimated to be 93.0 ± 42.2 μm, which is close to the size of raw Ti powders (~100 μm) and the TiB necklace structure. Notably, all the TiB particles are located at or near the prior β phase boundaries (**Figures 3g and 3h**), suggesting that the β-grain growth during solution treatment is effectively inhibited by the strong Zener pinning effect exerted by the TiB particles [68]. Furthermore, as observed from **Figure 3**, the morphology and distribution of TiB remain nearly unchanged, still presenting quasi-continuous necklace structure. This stability is attributed to the high

thermal stability of TiB, which is stable up to 1540 ºC (the eutectic temperature of Ti-B), and the extremely low solubility of B atoms in β-Ti at high temperatures (<0.02 at.%) [7].

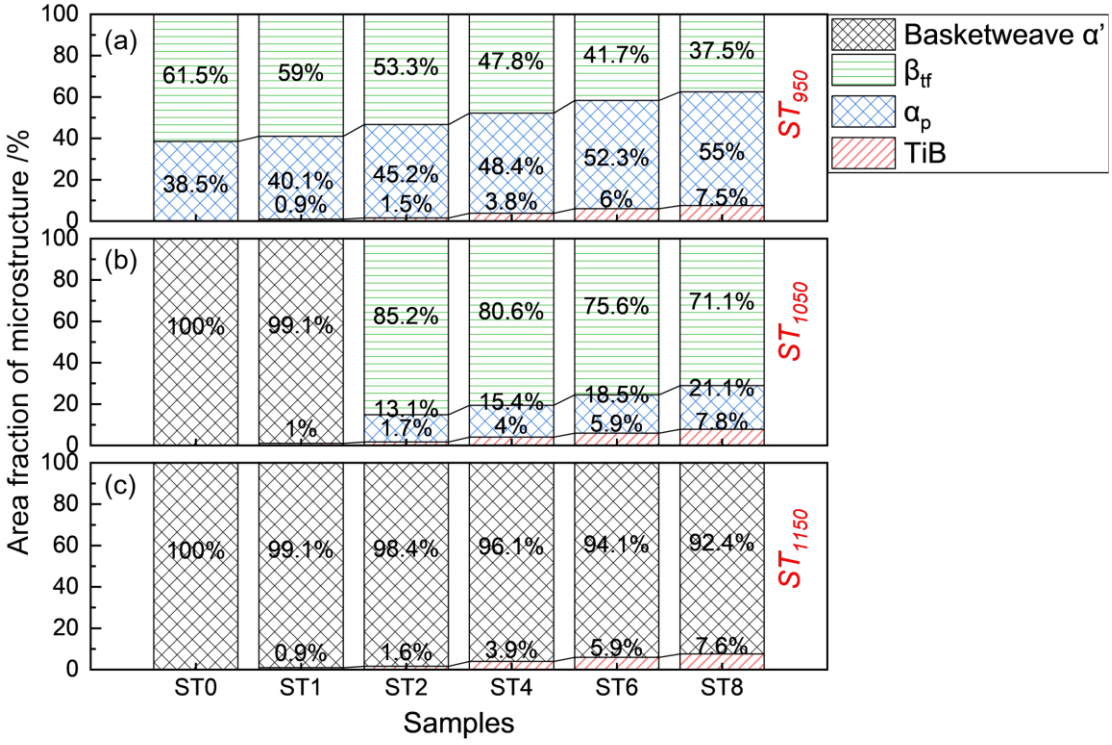


Figure 4. Area fractions of various microstructural constituents in the TiB/TA15 composites after solution treatment at (a) 950 °C, (b) 1050 °C, and (c) 1150 °C.

C. *Microstructure of solution treated and aged TiB/TA15 composites*

Figure 5 shows the representative microstructures of the $STA8_{500}$ and $STA8_{700}$ samples. After aging at 500 ℃ for 5 h, the matrix retains the basketweave structure composed of fine acicular α′, with no evidence of β-Ti formation. This is confirmed by the SAED images displayed in **Figure 5e**, indicating minimal α′ decomposition. These observations are consistent with the reported martensitic decomposition temperature (T_{dec}) of TA15 alloy, which lies above 600 ℃ [28, 44, 49, 50]. After aging at 700 ℃ for 5 h, extensive β-Ti ligament forms between α laths, and no significant grain coarsening is noted (**Figure 5d**). SAED analysis of the matrix in **Figure 5f** shows no evidence of ordered superlattice reflections in α-Ti, indicating the absence of α_2-Ti_3Al phase in both $STA8_{500}$ and $STA8_{700}$ samples.

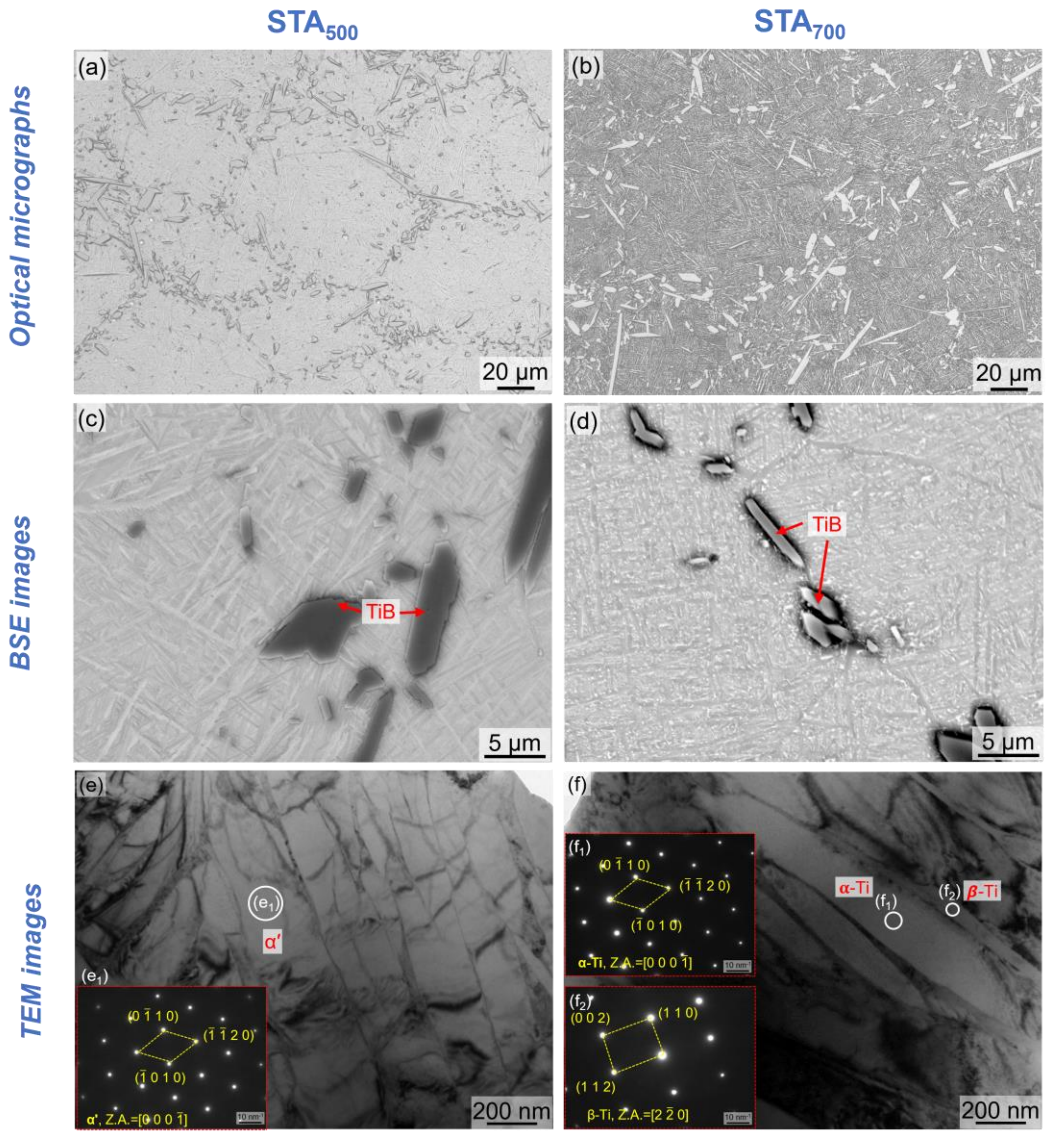


Figure 5. Representative microstructure of (a, c, e) STA8$_{500}$ and (b, d, f) STA8$_{700}$ samples: (a, b) OM, (c, d) SEM, (e, f) TEM images. The inserted (e1, f1, f2) images are SAED patterns.

D. *Mechanical properties*

1. *Uniaxial compression behavior*

Figure 6 shows the representative compressive stress–strain curves of as-sintered TMCs and variation of yield strength (σ_y) of all the TMCs. The values of compressive properties, including σ_y, ultimate compressive strength (σ_u), and strain to fracture(ε_f), are given in **Table S-II**. Compared to monolithic TA15 (S0), the introduction of 1 vol.% TiB notably enhances the yield strength, increasing from 0.68 to 1.18 GPa , with a 74% improvement. Further increases in TiB content gradually improves strength, but the

increment is not so significant as 1 vol.% addition, e.g., only 24.4% ($\Delta\sigma_y$ = 0.29 GPa) increment is achieved from S1 to S8. The ε_f decreases monotonically with increasing TiB content, mainly due to the densification of the TiB necklace, where TiB particles fracture prematurely and serve as crack nucleation sites during deformation [19, 20, 69].

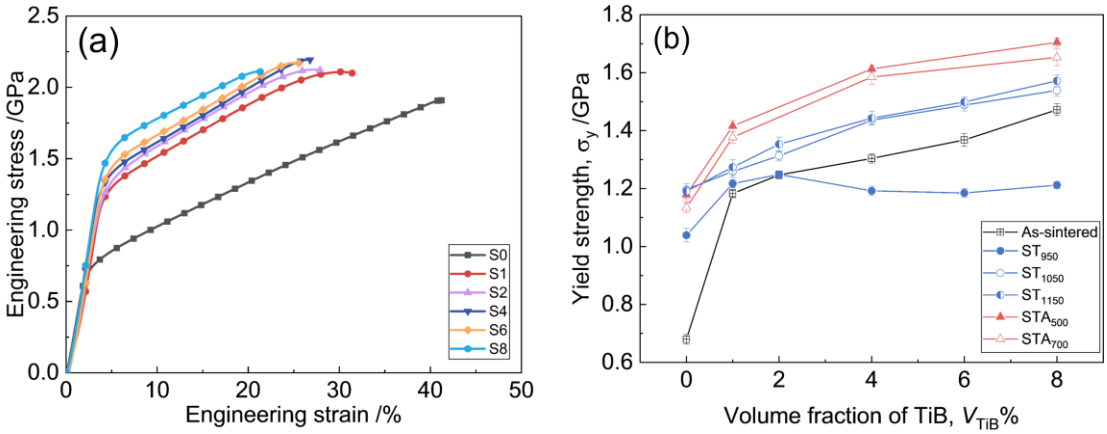


Figure 6. (a) Representative compressive stress–strain curves of as-sintered TiB/TA15 composites. (b) Variation of σ_y as a function of TiB volume fraction for all samples.

Representative stress-strain curves of ST and STA samples are shown in **Figures S4and S5**, respectively. The variations of σ_y of all TMCs are plotted in **Figure 6b**, and the values of compressive properties are given in **Tables S-II, S-III, and S-IV**. Among the three solution conditions, TMCs solution-treated at 950 °C exhibit the lowest σ_y ranging of about 1.19–1.22 GPa, slightly higher than unreinforced $ST0_{950}$ sample (1.02 GPa). TMCs solution-treated at 1050 and 1150 °C show comparable σ_y values, ranging from ~1.20 to 1.57 GPa. Notably, the 950 °C-treated TMCs display nearly identical σ_y despite having different TiB contents, which will be further discussed in **Section IV**. The ε_f of TMCs decreases with increasing solution temperature (**Table S-III**), while the σ_u remains relatively unaffected within the range of 1.91–2.19 GPa (**Figure 6b**).

Subsequent aging at 500 °C (after solution treatment at 1150 °C) results in the highest σ_y (~1.42–1.71 GPa) and σ_u (~2.03–2.28 GPa) among all tested samples (**Figure 6b**), while maintaining comparable ε_f (~13.2–15.5%) to solution-treated

specimens (**Table S-IV**). In particular, the $STA8_{500}$ sample exhibits the highest strength, with σ_y of ~1.71 GPa and σ_u of ~2.28 GPa (~40% higher than TA15 subjected to same treatment), while retaining a considerable ε_f of 13.2 ± 1.3% (slightly higher than that of TA15 alloy). Aging at 700 °C (after solution-treated at 1150 °C) leads to the martensitic decomposition and formation of β ligaments, resulting in a reduction in σ_y but increase in ε_f relative to the STA_{500} samples (**Figure 6b and Table S-IV**).

2. *Rockwell hardness*

Figure 7 presents the Rockwell hardness (HRA) values of all samples, which exhibit a trend similar to that of strength. For the as-sintered samples, HRA increases linearly with the TiB content, rising from 73.6 ± 0.7 to 82.1 ± 0.4 with an increment of 11.5%. With the exception of the ST_{950} treatment, both ST and STA treatments result in further hardness enhancement. The highest HRA value of 82.8 ± 0.2 is achieved in the $STA8_{500}$.

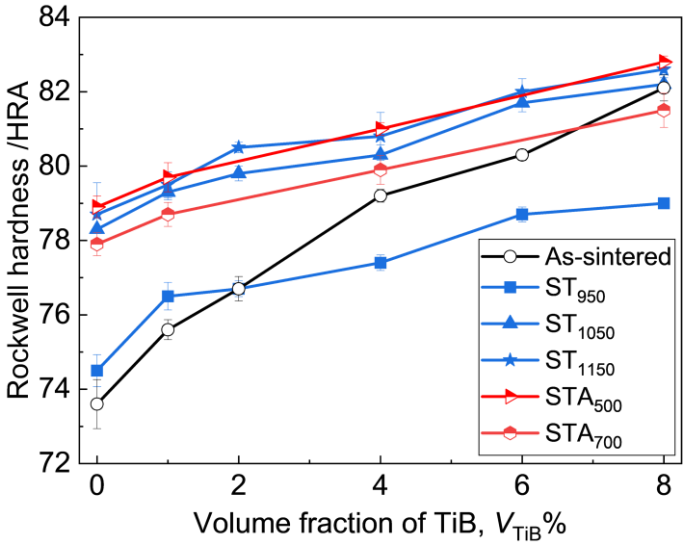


Figure 7. Rockwell hardness values of all TMCs samples.

IV. DISCUSSION

A. *Strengthening mechanisms in TMCs*

Strengthening mechanisms in metal matrix composites typically include: (1) solution strengthening ($\Delta\sigma_{ss}$) by alloying elements, (2) grain boundary strengthening

or Hall-Petch strengthening ($\Delta\sigma_{H\text{-}P}$) due to any grain refinement, and (3) dispersoid strengthening ($\Delta\sigma_{disper}$) introduced by the reinforcements [20, 37, 70]. $\Delta\sigma_{disper}$ is further comprises of strengthening caused by (a) the coefficient of thermal expansion (CTE) mismatch ($\Delta\sigma_{CTE}$), (b) additional stress required for dislocations to by-pass the particles ($\Delta\sigma_{Orowan}$), and (c) the load-sharing or load-transfer mechanism ($\Delta\sigma_{Load}$) [20, 71]. Additionally, strengthening caused by formation of geometrically necessary dislocations (GND) ($\Delta\sigma_{GND}$) is also considered in this work, which possibly arises from various processing techniques such as heat treatment and quenching.

The solid solution strengthening can be calculated based on the Fleischer model using Equations 2 and 3, which estimates the strengthening due to substitutional solutes (i.e., Al in this work) [72, 73]. The effect of B atoms on solid solution strengthening is neglected in this work, because the maximum solid solution of B in Ti is negligible [74] and almost all the added B result in the formation of TiB during sintering (No decomposition during heat treatment):

$$\Delta\sigma_{SS} = MG_m b\varepsilon_{ss}\sqrt{\Delta c} \tag{2}$$

$$\varepsilon_{ss} \approx \left|\frac{\varepsilon_G}{1+\left|\frac{\varepsilon_G}{2}\right|} - 3\varepsilon_\alpha\right| \tag{3}$$

where M is the mean orientation factor, G_m is the shear modulus of α-Ti, b is the magnitude of the Burgers vector of α-Ti, Δc is the atomic concentration increment of alloying element, and ε_{ss} is the interaction parameter that represents the combined effect of the atomic size and the shear modulus misfits. ε_G and ε_α are the lattice strains arising from atomic size and the shear modulus misfits, respectively.

The Hall-Petch relationship is applied to estimate the strength increment caused by the grain refinement, which is expressed as Equation 4 [75]:

$$\Delta\sigma_{\text{H-P}} = K\left(d_2^{-0.5} - d_1^{-0.5}\right) \tag{4}$$

where K is the Hall-Petch coefficient reflecting the magnitude of hardening due to grain boundaries and d_1 and d_2 are the average grain sizes of the composite material before and after grain refinement, respectively. In this study, $\Delta\sigma_{H\text{-}P}$ was estimated

using the colony size for lamellar structure and α-lath width for basketweave structure, as these correspond to characteristic high-angle boundaries that effectively impede the dislocation movement [19, 76-79].

The contribution of thermal mismatch strengthening, arising from the difference in thermal expansion coefficients between ceramic particles and the metallic matrix, can be calculated using Equation 5 [80]. The addition of TiB induced $\Delta\sigma_{CTE}$ is generally negligible compared to other reinforcements, as the CTE values between TiB and Ti are very close ($CTE_{Ti} = 9 \times 10^{-6}$ K^{-1}, $CTE_{TiB} = 8.6 \times 10^{-6}$ K^{-1}) [7].

$$\Delta\sigma_{CTE} = \sqrt{3}\beta G_m b\sqrt{\rho_{CTE}} = \sqrt{3}\beta G_m\sqrt{\frac{12V_{TiB}\%\Delta\alpha\Delta T}{bd}} \#(5)$$

where β is the dislocation strengthening coefficient, ρ_{CTE} is the density of dislocations generated from the CTE difference, $V_{TiB}\%$ is the volume fraction of TiB, ΔT is the temperature change, $\Delta\alpha$ is the CTE difference between the matrix and the reinforcement, and d is the diameter of reinforcement.

Particle strengthening ($\Delta\sigma_{Orowan}$) caused by the resistance of closely spaced hard particles (within grains) to the movement of dislocations is important in many TMCs and dispersion strengthened alloys [81, 82]. Their contribution is usually given by the Orowan-Ashby Equation 6 [70, 82, 83], which is inversely proportional to the interparticle spacing and can be estimated using Equation 7.This indicates that particles with small diameter and close spacing provide more strengthening. As the TiB particles in TiB/TA15 composites are mainly located near the colony/grain boundaries and are in micro-scale [19], the strengthening caused by them is generally negligible.

$$\Delta\sigma_{Orowan} = \frac{0.13G_m b}{\lambda} ln\frac{d_p}{2b} \#(6)$$

$$\lambda \approx d_p\left[\left(\frac{1}{2V_{TiB}\%}\right)^{\frac{1}{3}} - 1\right] \#(7)$$

where G_m is the shear modulus of matrix, λ is the interparticle spacing, and d_p is the average diameter of the particles.

With limited influence on the dislocation movement, it is important to consider the contribution of reinforcements on $\Delta\sigma_{Load}$ [81], which can be caused by the high elastic modulus (and stiffness) of TiB and the strong interface between TiB and α-Ti. It can be generally expressed as Equation 8 based on the generalized shear-lag model [11, 23, 84]:

$$\Delta\sigma_{Load} = 0.5\,\sigma_m\,l\,V_{TiB}\%\#(8)$$

where σ_m is the yield strength of the matrix and l is the aspect ratio of TiB.

Taking into account the formation of TiB 'necklace', which increased the local $V_{\mathrm{TiB}}\%$ and commonly observed typically in the TMCs manufactured using the powder metallurgy technique, $V_{TiB}\%$ can be modified as following Equation (9) [11, 85]:

$$(V_{TiB}\%)_m = \frac{1}{1 - \left(1 - \frac{L}{R}\right)^3} V_{TiB}\%\#(9)$$

where $(V_{TiB}\%)_m$ is modified $V_{TiB}\%$, L and R are the thickness and radius of the network, respectively. The upper bound of $\Delta\sigma_{Load}$ is essentially marked-up with the usage of modified $V_{TiB}\%$ [16].

Additionally, the strengthening contribution from the formation of GNDs ($\Delta\sigma_{GND}$) can be estimated using the Bailey-Hirsch relationship [23, 86] given by Equation 10. The density of GNDs (ρ_{GND}) can be approximated based on KAM values obtained from the EBSD analysis and using Equation 11 [87, 88]. It should be noted that this approach underestimates the total dislocation density and thus the associated strengthening contribution, since statistically stored dislocations (SSDs) are not accounted for here.

$$\Delta\sigma_{GND} = M\alpha G_m b\sqrt{\rho_{GND}}\#(10)$$

$$\rho_{GND} = \frac{2KAM}{\mu b}\#(11)$$

where M is the Taylor factor, α is a constant reflecting dislocation interactions, ρ_{GND} is the GND density, and μ is the step size of EBSD scan.

In literature, the following three methods are widely adopted for estimating the total strength contribution from the aforementioned mechanisms to metal matrix

composite materials [37, 70]. (i) Arithmetic summation, expressed by Equation 12, which assumes that each mechanism acts independently and contributes additively to the overall yield strength of composite, i.e., there is no synergy between the mechanisms. (ii) Quadratic summation, given by Equation 13, which was proposed by Clyne and co-workers [38] for composites reinforced with micro-sized reinforcements and assumes the square of total strength increment is equal to the sum of squares of each contribution. (iii) Compounding method, described by Equation 14, which treats each mechanism as a multiplicative factor and their combined effect accumulates progressively [70].

$$\Delta\sigma_{arithmetic} = \Delta\sigma_{ss} + \Delta\sigma_{H-P} + \Delta\sigma_{CTE} + \Delta\sigma_{Orowan} + \Delta\sigma_{Load} + \Delta\sigma_{GND} \#(12)$$

$$\Delta\sigma_{quadratic} = \sqrt{(\Delta\sigma_{ss})^2 + (\Delta\sigma_{H-P})^2 + (\Delta\sigma_{CTE})^2 + (\Delta\sigma_{Orowan})^2 + (\Delta\sigma_{Load})^2 + (\Delta\sigma_{GND})^2} \#(13)$$

$$\Delta\sigma_{compounding} = \sigma_m \left[\begin{array}{c} \left(1 + \frac{\Delta\sigma_{ss}}{\sigma_m}\right) \times \left(1 + \frac{\Delta\sigma_{H-P}}{\sigma_m}\right) \times \left(1 + \frac{\Delta\sigma_{CTE}}{\sigma_m}\right) \times \left(1 + \frac{\Delta\sigma_{Orowan}}{\sigma_m}\right) \times \\ \left(1 + \frac{\Delta\sigma_{Load}}{\sigma_m}\right) \times \left(1 + \frac{\Delta\sigma_{GND}}{\sigma_m}\right) - 1 \end{array} \right] \#(14)$$

where $\Delta\sigma_m$ is the yield strength of baseline sample.

Taking the unreinforced TA15 alloy (S0) as the baseline, the strengthening contributions of individual mechanisms were calculated for as-sintered TMCs (S1–S8) and are displayed in **Figure 8a**. A comparison between the predicted strength increment ($\Delta\sigma_{Theory}$) and the experimentally measured yield strength increment ($\Delta\sigma_{Test}$) is presented in **Figure 8b**. The numerical constants (e.g., *K*, G_m, and *b* [20, 72, 87-91]) and microstructural parameters (e.g., ρ_{GND}, diameter and aspect ratio of TiB) used in strengthening calculations are summarized in **Tables S-V and S-VI**.

Among all the mechanisms, $\Delta\sigma_{Load}$ is found to be the dominant contributor, followed by $\Delta\sigma_{H\text{-}P}$ (**Figure 8a**), which is consistent with prior reports [57, 92]. However, all three theoretical summation methods significantly underestimate the strength increment compared to experimental results. Similar deviations have also been reported in other TiB/TMCs [14, 20, 61, 93]. This discrepancy is mainly attributed to pronounced matrix microstructural changes induced by minor additions

of TiB or B, such as transformation from lamellar to equiaxed microstructures, elimination of grain boundary α, and drastic grain refinement [19, 56].

To account for this, a revised benchmark using the S1 composite (with minimal TiB addition) is employed. The recalculated strengthening contributions and comparisons are demonstrated in **Figures 8c and 8d**. This approach eliminates the pronounced microstructural transition observed from S0 to S1 and provides a more accurate assessment of strengthening due solely to increase in the TiB content. Given the comparable grain sizes across S1–S8 (ranging from 41–26 μm, see **Figure 2a**), the contribution from $\Delta\sigma_{H\text{-}P}$ is relatively small, reaffirming load transfer as the dominant strengthening mechanism. Furthermore, the similar α/β phase morphology and volume fraction (**Figure 2b**) across these samples minimizes the effect of matrix microstructural differences. Consequently, the predicted yield strengths, particularly those based on the quadratic summation method, exhibit reasonable agreement with the experimental values (**Figure 8d**).

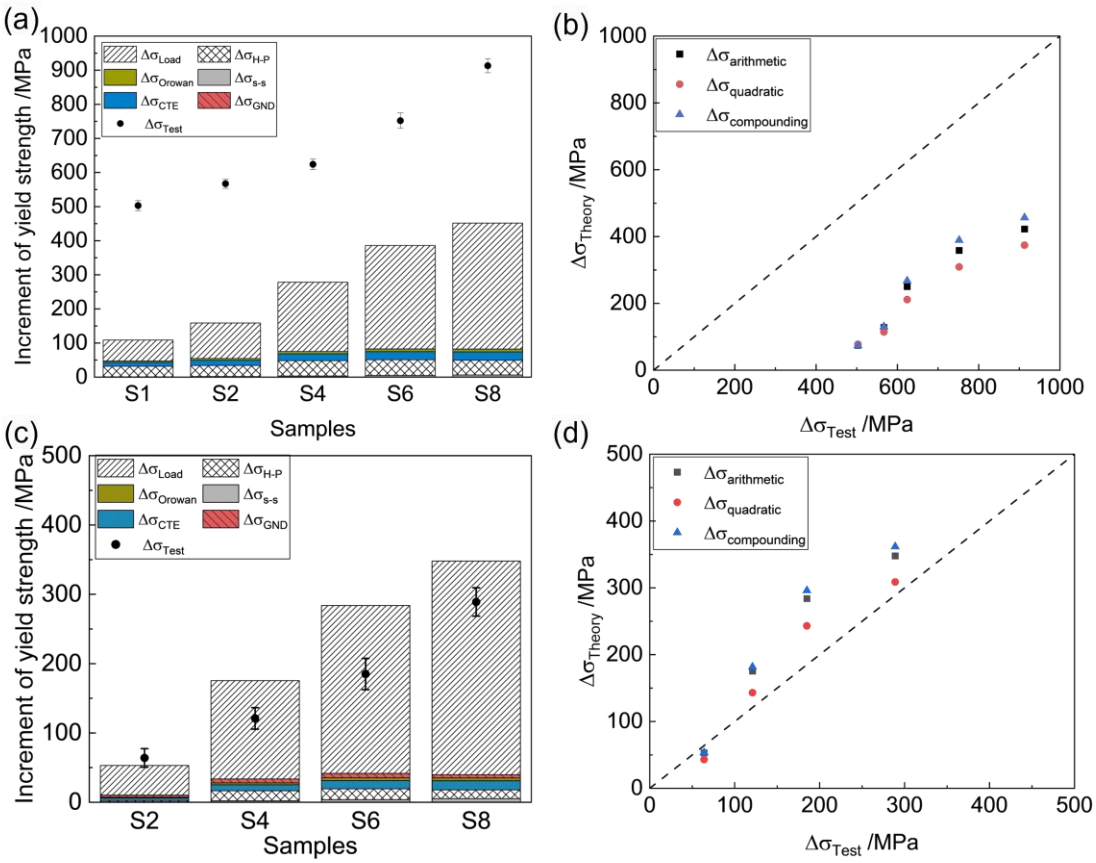


Figure 8. Strengthening mechanism analysis for as-sintered TiB/TA15 composites. (a, c)

Estimated contributions of individual strengthening mechanisms to the yield strength increment, benchmarked against (a) unreinforced TA15 (S0) and (c) S1 composite. (b, d) Comparison between experimental and theoretical yield strength improvements using arithmetic, quadratic, and compounding summation methods based on (b) S0 and (d) S1 as the reference. Results highlight the dominant role of load-transfer strengthening and improved predictive accuracy when matrix microstructural effects are minimized (S1 as baseline).

B. *Effect of matrix microstructure on strengthening in TMCs*

The evaluation of the strengthening contributions provided in the previous section clearly shows that the load-transfer is the dominant mechanism for all TMCs (S1–S8). To further assess the strengthening efficiency of the TiB reinforcements, the yield strength of composites with different matrices was plotted as a function of effective TiB volume fraction (V_{TiB}%), as defined in Equation 8, and presented in **Figure 9**. The slope of the resulting linear fit, denoted as k_{YS}, represents the yield strength increment per 1vol.% TiB addition. Interestingly, k_{YS} values are relatively consistent across most matrix conditions, ranging from 37.8 to 41.1 MPa/vol.%, except for the ST_{950} samples, which shows a negative k_{YS} (−4.2 MPa/vol.%), indicating negligible strengthening despite increasing TiB content. This anomaly highlights the influence of matrix microstructure. Additionally, the good linear correlation observed among samples S1–S8, regardless of the presence of coherent α_2-Ti_3Al phase, suggests that strengthening contribution from the α_2 phase is negligible compared to that of the TiB particles.

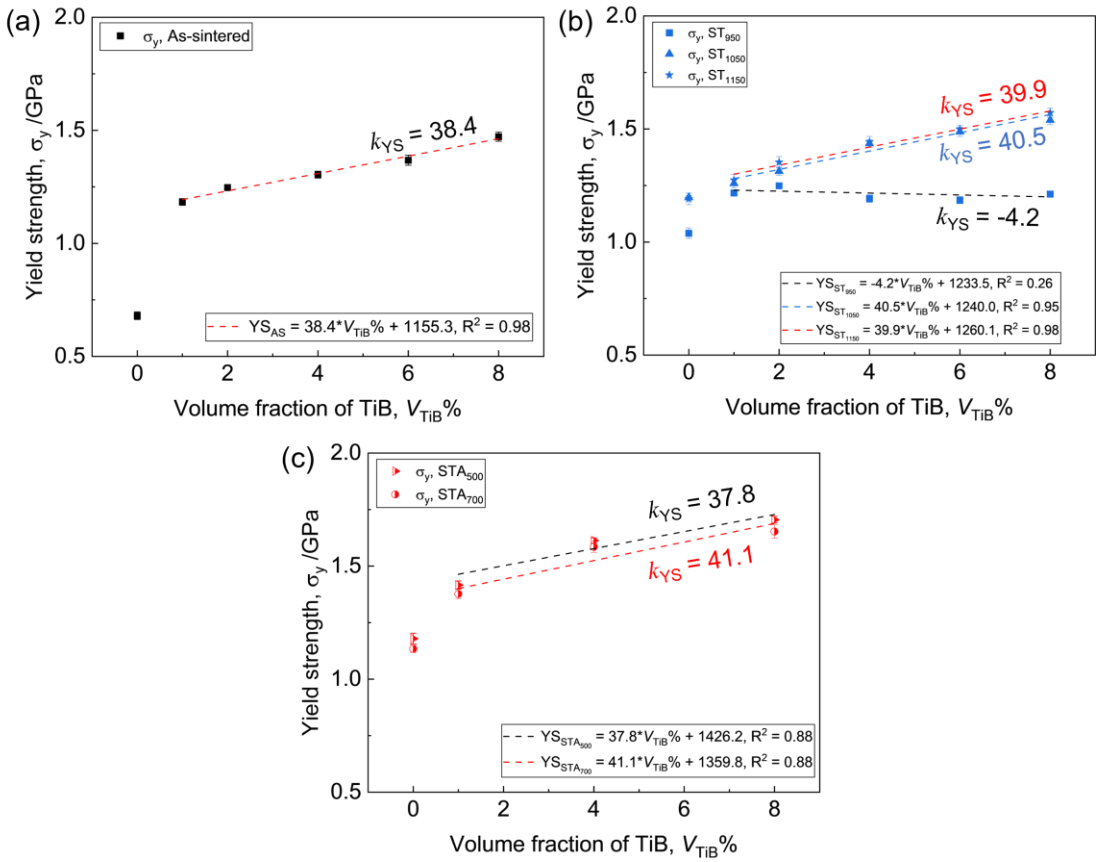


Figure 9. Strengthening efficiency analysis as a function of V_{TiB}% in TiB/TA15 composites for: (a) as-sintered condition, (b) solution treated condition, and (c) solution treated and aged condition.

To investigate the matrix effect, Vickers hardness measurements were performed on ST_{950} and ST_{1150} samples, and the results are presented in **Figure 10a**. The β_{tf} phase exhibits ~20% higher hardness than primary α_p, and comparable hardness to martensitic α′ (within ~5% difference). These results suggest that the enhanced yield strengths observed in ST_{1050} (β_{tf} dominated) and ST_{1150} (α′ dominated) composites, relative to as-sintered ones (α_p dominated), can be primarily attributed to matrix hardening. The matrix hardening is likely driven by the following three synergistic mechanisms. (1) Hall–Petch strengthening from grain refinement (~41–26 μm in as-sintered samples to ~4.8 μm in ST samples). (2) Solid solution strengthening due to supersaturation of multiple alloying elements. (3) Dislocation strengthening induced by rapid quenching. The relative proportions of two 'harder' phases (TiB and β_{tf},) in ST_{950} are plotted in **Figure 10b**. With increasing V_{TiB}%, a decreasing trend of β_{tf} proportion is observed. This trade-off between V_{TiB}% and β_{tf} results in an overall

near-identical hard-phase fraction, thereby explaining the almost constant yield strength across all ST_{950} samples. In contrast, under other heat treatment conditions, as well as in the as-sintered state, the matrix microstructures exhibit same morphology, comparable grain sizes, similar proportions of hard phases, or consistent hardness values across samples. This minimizes the influence of matrix differences and highlights the predominant role of TiB volume fraction in strengthening.

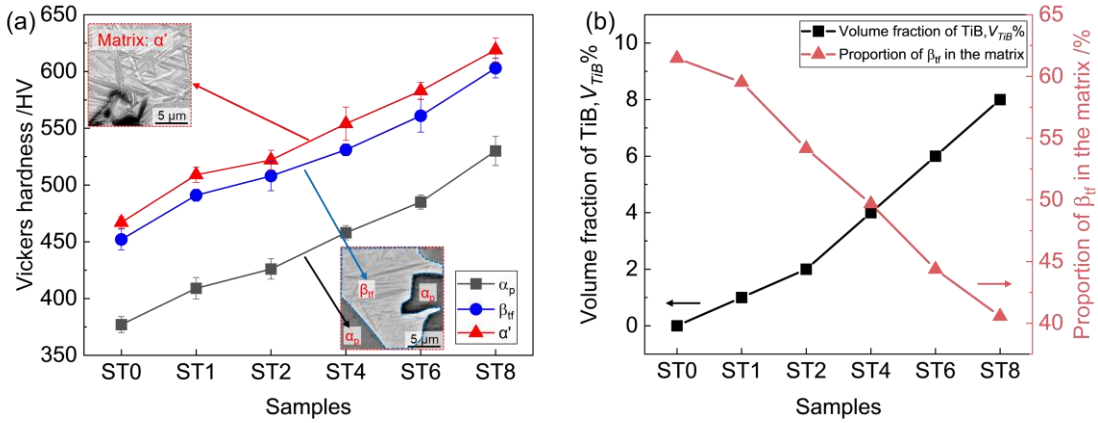


Figure 10. (a) Vickers hardness of the matrix in ST_{950} and ST_{1150} samples, with representative microstructures shown in insets. (b) TiB volume fraction and β_{tf} proportion ($V_{\beta tf}/(V_{\beta tf} + V_{\alpha})$) in the matrix for ST_{950} samples.

C. *Phase evolution during cooling*

With the assistance of JMatPro software, the schematic continuous cooling transformation (CCT) diagram for TiB/TA15 composites was constructed (**Figure 11**) to illustrate the evolution of matrix microstructures and summarize their mechanical properties under different cooling paths. Since TiB is thermodynamically stable up to ~1540 ºC (the eutectic temperature between Ti and B [7]), its morphology and distribution remains largely unaffected by the cooling conditions either during powder metallurgy or subsequent heat treatments. Therefore, the diagram emphasizes the transformation of the Ti matrix and the effect of TiB on its evolution. (**Path 1**) When solution-treated below T_{β}, only partial dissolution of primary α occurs. Upon rapid cooling (e.g., water quenching, ~8000 ºC/min [94]), secondary α laths precipitate within the β phase, forming a β_{tf} structure through an analogous martensitic transformation. (**Path 2**) For the samples solution-treated above T_{β}, all the α-Ti phase

dissolves into β-Ti, forming a prior-β grain structure whose boundaries are pinned by the TiB particles. Fast cooling (i.e., water quenching) then triggers diffusionless martensitic transformation (β → α′), leading to the formation of acicular α′ martensite. (**Path 3**) Subsequent aging above T_{dec} followed by air cooling (~100 ºC/min [94]) on samples subjected to Path 2, results in the martensitic decomposition (α′→ α + β) without significant grain coarsening, forming acicular α + β microstructure. (**Path 4**) During hot-press sintering, the in-situ reaction (AlB_2 + 2Ti → 2TiB + Al) proceeds more thoroughly [95], and α-Ti forms via heterogenous nucleation with the help of TiB and undergoes full recrystallization during the slow furnace cooling (~1 ºC/min [94]), producing an equiaxed α+β structure. Additionally, slow cooling also promotes the precipitation of α_2-Ti_3Al in the TMCs with a high Al content.

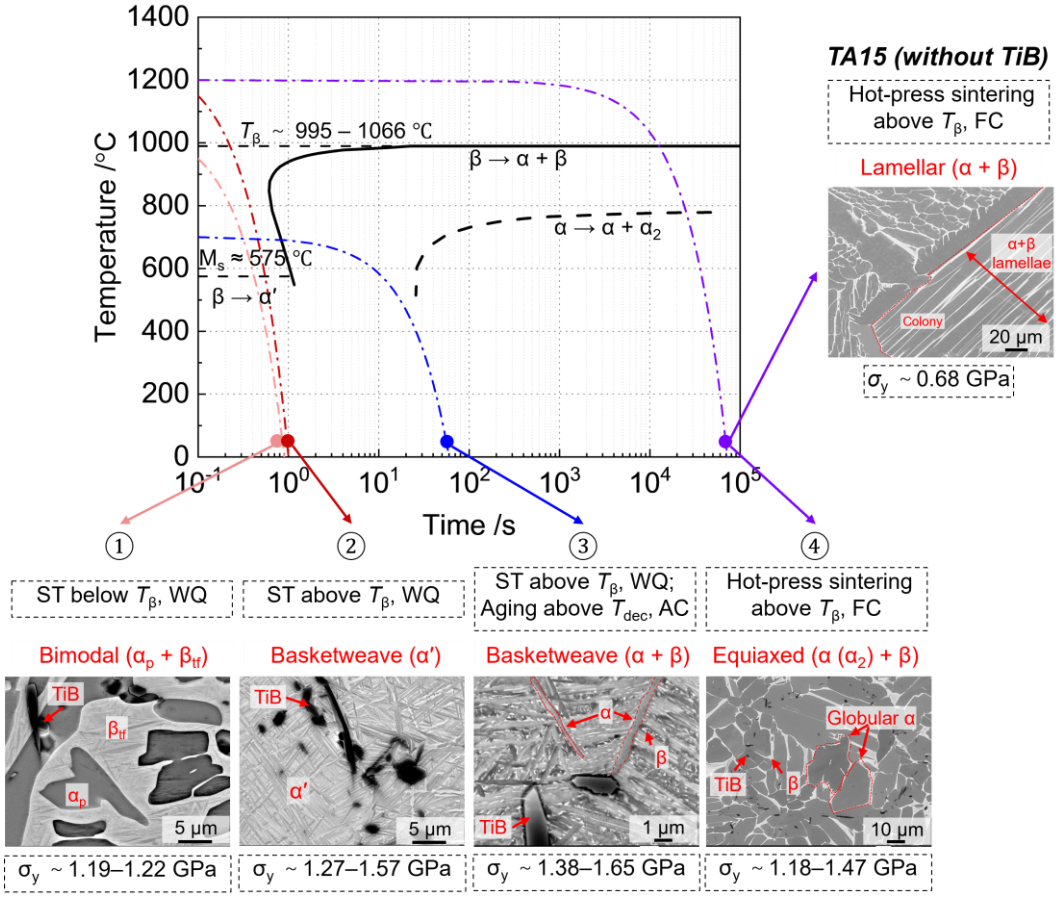


Figure 11. Schematic continuous cooling transformation (CCT) diagram for TiB/TA15 composites, illustrating four representative microstructures formed under different cooling conditions and their mechanical properties. Colored dot-dash lines indicate the cooling paths. ST,

solution treatment; HP, hot pressing; WQ, water quenching; AC, air cooling; FC, furnace cooling. (For reference only, the martensite start temperature (M_s) of Ti-6Al-4V is marked, taken from Ref. [96])

Before closing, it is important to emphasize the critical role of matrix microstructure—particularly the relative fractions of different phases/microstructures—in governing the strength of TiB-reinforced dual-phase TMCs. In principle, strengthening contributions should be weighted by their respective proportions, especially for α_p and β_{tf} in bimodal structures. In the present work, however, we did not attempt to quantitatively resolve these contributions. Instead, we focused on highlighting the significance of matrix effects through an initial experimental exploration, an aspect often overlooked in the TMC literature. A more comprehensive understanding may benefit from integrated approaches, such as detailed microstructural quantification, micromechanical simulations of load sharing and strain partitioning, and new predictive modeling. Such efforts will be essential for establishing robust design principles that explicitly leverage matrix microstructure as a key parameter for optimizing the performance of TMCs.

V. SUMMARY

In this study, a series of TiB-reinforced (0–8 vol.%) dual-phase titanium matrix composites (TMCs) were successfully fabricated through powder metallurgy and subsequent heat treatments following different protocols, resulting in various matrix microstructures, including equiaxed, lamellar, bimodal, and basketweave. The corresponding strengthening mechanisms were systematically analyzed as a function of TiB volume fraction and matrix microstructure. Furthermore, a schematic continuous cooling transformation diagram was constructed. The key conclusions are summarized below.

1. Strengthening mechanism due to TiB additions. Quantitative analysis reveals that even minimal TiB additions result in a significant increase in strength, most likely due to matrix microstructural changes that are not fully captured by conventional

models. With an increasing TiB content, load transfer becomes the dominant strengthening mechanism, followed by the Hall–Petch strengthening. Theoretical predictions, particularly those based on the quadratic summation method, show good agreement with experimental results.

2. Heat treatment induced microstructure and strength evolution. The β-transus temperature (T_β) of the TMCs increases with AlB_2 addition, attributed to the strong α-stabilizing effect of Al. Below T_β, solution treatment transforms the equiaxed α + β matrix into a mixture of transformed β and primary α; above T_β, it produces acicular martensitic α′. Subsequent aging above the martensitic decomposition temperature (T_{dec}) decomposes α′ into α + β. Solutionization enhance matrix strength significantly due to the formation of harder phases (transformed β or α′), grain refinement, solid solution strengthening, and increased dislocation density; however, aging causes a slight reduction in strength due to α′ decomposition.

3. Strengthening efficiency of TiB additions. The strengthening efficiency, defined as the yield strength increment per 1 vol.% TiB addition, remains relatively consistent across different matrix microstructures (~37.8–41.1 MPa/vol.%) when the matrix morphology is similar. In composites containing a mixture of soft and hard phases (e.g., β_{tf} and α′), the overall yield strength is further influenced by the volume fraction of the harder phase, in addition to the TiB content.

ACKNOWLEDGEMENTS

This work was supported by National Natural Science Foundation of China (Grants No W2411048, 52271042) and the National Key Research and Development Program of China (2021YFB3701204). YZ acknowledges the support by FEAT Strategic Research and Translational Thrust. We thank Instrumental Analysis Center of Xi'an Jiaotong University and Dr. Chaowei Guo and Dr. Chuanwei Fan from CAMP-Nano for technical support.

DECLARATION OF INTEREST STATEMENT

The authors declare that they have no known competing financial interests or personal relationships that could have appeared to influence the work reported in this

paper.

CREDIT AUTHORSHIP COMTRIBUTION STATEMENT

Zheyu Miao: Data curation, Investigation, Visualization, Writing- Original draft. **Yu Chen**: Data curation, Investigation, Resources. **Qiang Li**: Conceptualization, Methodology, Validation, Formal analysis, Supervision, Writing- Reviewing and Editing. **Yakai Zhao:** Writing- Reviewing and Editing. **Kai Chen:** Funding acquisition, Resources, Writing- Reviewing and Editing. **Yimin Gao:** Supervision, Funding acquisition, Resources, Project administration. **Upadrasta Ramamurty:** Supervision, Resources, Writing- Reviewing and Editing.

REFERENCE

1. Manfred Peters and Christoph Leyens: *Titanium and titanium alloys: fundamentals and applications*. John Wiley and Sons, New York, 2006.
2. E. T. Zhao, S. C. Sun, and Y. Zhang: *Journal of Materials Research and Technology-Jmr&T* 2021, vol. 14, pp. 3029-42. http://dx.doi.org/10.1016/j.jmrt.2021.08.117
3. M. D. Hayat, H. Singh, Z. He, and P. Cao: *Compos. Pt. A-Appl. Sci. Manuf.* 2019, vol. 121, pp. 418-38. http://dx.doi.org/10.1016/j.compositesa.2019.04.005
4. Indrani Sen and U. Ramamurty: *Scr. Mater.* 2010, vol. 62, pp. 37-40. http://dx.doi.org/10.1016/j.scriptamat.2009.09.022
5. S. Gorsse, Y. Le Petitcorps, S. Matar, and F. Rebillat: *Mat Sci Eng a-Struct* 2003, vol. 340, pp. 80-87. http://dx.doi.org/10.1016/S0921-5093(02)00188-0
6. K. S. R. Chandran, K. B. Panda, and S. S. Sahay: *JOM* 2004, vol. 56, pp. 42-48. http://dx.doi.org/10.1007/s11837-004-0127-1
7. G. Singh and U. Ramamurty: *Prog Mater Sci* 2020, vol. 111, p. 100653. http://dx.doi.org/10.1016/j.pmatsci.2020.100653
8. W. J. Lu, D. Zhang, X. N. Zhang, R. J. Wu, T. Sakata, and H. Mori: *J. Alloys Compd.* 2001, vol. 327, pp. 240-47. http://dx.doi.org/10.1016/S0925-8388(01)01445-1
9. Y. F. Yang, M. Yan, S. D. Luo, G. B. Schaffer, and M. Qian: *J. Alloys Compd.* 2013, vol. 579, pp. 553-57. http://dx.doi.org/10.1016/j.jallcom.2013.07.097
10. L. J. Huang, L. Geng, B. Wang, and L. Z. Wu: *Materials & Design* 2013, vol. 45, pp. 532-38. http://dx.doi.org/10.1016/j.matdes.2012.09.043
11. Q. Li, Y. Chen, X. Y. Huang, Y. R. Wang, Y. K. Zhao, U. Ramamurty, and Y. M. Gao: *Mat Sci Eng a-Struct* 2022, vol. 841, p. 143021. http://dx.doi.org/10.1016/j.msea.2022.143021
12. M. Y. Koo, J. S. Park, M. K. Park, K. T. Kim, and S. H. Hong: *Scr. Mater.* 2012, vol. 66, pp. 487-90. http://dx.doi.org/10.1016/j.scriptamat.2011.12.024
13. D. Pan, X. Zhang, X. D. Hou, Y. F. Han, M. Q. Chu, B. Chen, L. Jia, K. Kondoh, and S. F. Li: *Mat Sci Eng a-Struct* 2021, vol. 799, p. 140137. http://dx.doi.org/10.1016/j.msea.2020.140137
14. H. D. Wu, Y. F. Han, J. W. Le, N. Zong, S. P. Li, Y. F. Luo, G. F. Huang, J. W. Mao, and W. J. Lu: *J. Alloys Compd.* 2022, vol. 915. http://dx.doi.org/10.1016/j.jallcom.2022.165399
15. L. Liu, S. F. Li, X. Zhang, S. L. Li, S. D. Wang, B. Li, L. N. Gao, H. Y. Liu, D. X. Hui, D. Pan, S. Kariya, J. Umeda, and K. Kondoh: *Compos Part B-Eng* 2024, vol. 276. http://dx.doi.org/10.1016/j.compositesb.2024.111366
16. L. J. Huang, L. Geng, and H. X. Peng: *Prog Mater Sci* 2015, vol. 71, pp. 93-168. http://dx.doi.org/10.1016/j.pmatsci.2015.01.002
17. L. Q. Huang, L. H. Wang, M. Qian, and J. Zou: *Scr. Mater.* 2017, vol. 141, pp. 133-37. http://dx.doi.org/10.1016/j.scriptamat.2017.08.007
18. H. Q. Liu, M. H. Fang, Y. F. Han, G. F. Huang, Z. G. Sun, L. Zhang, and W. J. Lu: *Compos Part B-Eng* 2023, vol. 262. http://dx.doi.org/10.1016/j.compositesb.2023.110822
19. Q. Li, S. Huang, Y. M. Gao, and U. Ramamurty: *Mat Sci Eng a-Struct* 2024, vol. 916. http://dx.doi.org/10.1016/j.msea.2024.147351

20. Q. Li, S. Huang, Y. K. Zhao, Y. M. Gao, and U. Ramamurty: *Acta Mater.* 2023, vol. 254, p. 118995. http://dx.doi.org/10.1016/j.actamat.2023.118995
21. Y. Jiao, L. J. Huang, L. Geng, X. T. Li, Y. N. Gao, M. F. Qian, and R. Zhang: *Materials Science and Engineering: A* 2017, vol. 701, pp. 359-69. http://dx.doi.org/10.1016/j.msea.2017.06.067
22. X. Chen, L. J. Huang, S. Ma, F. B. Sun, S. Wang, and L. Geng: *Journal of Materials Science & Technology* 2025, vol. 206, pp. 1-14. http://dx.doi.org/10.1016/j.jmst.2024.03.062
23. Shaolou Wei, Lujun Huang, Xinting Li, Yang Jiao, Wei Ren, and Lin Geng: *Metall Mater Trans A* 2019, vol. 50, pp. 3629-45. http://dx.doi.org/10.1007/s11661-019-05244-7
24. C. J. Zhang, J. P. Qu, J. Wu, S. Z. Zhang, J. C. Han, M. D. Hayat, and P. Cao: *Mater. Lett.* 2018, vol. 233, pp. 242-45. http://dx.doi.org/10.1016/j.matlet.2018.09.012
25. Y. Jiao, L. J. Huang, L. Geng, R. Zhang, S. Jiang, X. T. Li, and Y. N. Gao: *Powder Technol.* 2019, vol. 356, pp. 980-89. http://dx.doi.org/10.1016/j.powtec.2019.09.008
26. B. Wang, L. J. Huang, and L. Geng: *Mat Sci Eng a-Struct* 2012, vol. 558, pp. 663-67. http://dx.doi.org/10.1016/j.msea.2012.08.071
27. H. T. Hu, L. J. Huang, L. Geng, C. Liu, and B. Wang: *J. Alloys Compd.* 2014, vol. 582, pp. 569-75. http://dx.doi.org/10.1016/j.jallcom.2013.08.095
28. R. Zhang, D. J. Wang, L. J. Huang, and S. J. Yuan: *Mat Sci Eng a-Struct* 2017, vol. 679, pp. 314-22. http://dx.doi.org/10.1016/j.msea.2016.10.041
29. R. Zhang, K. Xu, F. B. Sun, Z. S. Ma, L. J. Huang, L. Bolzoni, L. Geng, and F. Yang: *Mater. Charact.* 2024, vol. 212. http://dx.doi.org/10.1016/j.matchar.2024.113978
30. B. Wang, L. J. Huang, L. Geng, and Z. S. Yu: *J. Alloys Compd.* 2017, vol. 690, pp. 424-30. http://dx.doi.org/10.1016/j.jallcom.2016.08.138
31. B. Wang, L. J. Huang, L. Geng, X. D. Rong, and B. X. Liu: *Materials & Design* 2015, vol. 85, pp. 679-86. http://dx.doi.org/10.1016/j.matdes.2015.07.058
32. S. P. Li, Y. F. Han, Z. S. Shi, G. F. Huang, N. Zong, J. W. Le, P. K. Qiu, and W. J. Lu: *Mater. Charact.* 2020, vol. 168. http://dx.doi.org/10.1016/j.matchar.2020.110527
33. Orest M. Ivasishin, Roman V. Teliovych, Volodymyr G. Ivanchenko, Seshacharyulu Tamirisakandala, and Daniel B. Miracle: *Metall Mater Trans A* 2007, vol. 39, pp. 402-16. http://dx.doi.org/10.1007/s11661-007-9425-x
34. C. X. Wang, T. X. Zhou, T. Wu, M. G. Zhang, J. F. Wu, X. H. Xu, L. Q. Zhan, J. H. Wang, and G. F. Wang: *J. Alloys Compd.* 2025, vol. 1036. http://dx.doi.org/10.1016/j.jallcom.2025.182017
35. Guangfa Huang, Yuanfei Han, Xianglong Guo, Di Qiu, Liqiang Wang, Weijie Lu, and Di Zhang: *Materials Science and Engineering: A* 2017, vol. 688, pp. 155-63. http://dx.doi.org/10.1016/j.msea.2017.02.002
36. Zhenlun Li, Qingxin Kang, Xiaochong Sui, Xunhu Xu, Liqiang Zhan, and Guofeng Wang: *Journal of Materials Science & Technology* 2023, vol. 167, pp. 137-51. http://dx.doi.org/10.1016/j.jmst.2023.05.023
37. M. Y. Zhou, L. B. Ren, L. L. Fan, Y. W. X. Zhang, T. H. Lu, G. F. Quan, and M. Gupta: *J. Alloys Compd.* 2020, vol. 838, p. 155274. http://dx.doi.org/10.1016/j.jallcom.2020.155274
38. T. W. Clyne and P. J. Withers: *An Introduction to Metal Matrix Composites*. Cambridge

University Press, 2010.

39. Ruyi Ji, Kai Zhu, Haicheng Zhang, Hengjun Luo, and Jian Mao: *J. Mater. Res. Technol.* 2024, vol. 28, pp. 1644-56. http://dx.doi.org/10.1016/j.jmrt.2023.12.099

40. P. F. Gao, G. Qin, X. X. Wang, Y. X. Li, M. Zhan, G. J. Li, and J. S. Li: *Materials Science and Engineering: A* 2019, vol. 739, pp. 203-13. http://dx.doi.org/10.1016/j.msea.2018.10.030

41. H. R. Zhang, H. Z. Niu, M. C. Zang, H. Tan, and D. L. Zhang: *Materials Science and Engineering: A* 2021, vol. 825. http://dx.doi.org/10.1016/j.msea.2021.141902

42. Y. Chong, G. Y. Deng, S. Gao, J. H. Yi, A. Shibata, and N. Tsuji: *Scr. Mater.* 2019, vol. 172, pp. 77-82. http://dx.doi.org/10.1016/j.scriptamat.2019.07.015

43. Z. Guo, S. Malinov, and W. Sha: *Computational Materials Science* 2005, vol. 32, pp. 1-12. http://dx.doi.org/10.1016/j.commatsci.2004.05.004

44. Chao Cai, Xu Wu, Wan Liu, Wei Zhu, Hui Chen, Jasper Chua Dong Qiu, Chen-Nan Sun, Jie Liu, Qingsong Wei, and Yusheng Shi: *Journal of Materials Science & Technology* 2020, vol. 57, pp. 51-64. http://dx.doi.org/10.1016/j.jmst.2020.05.004

45. P. K. Qiu, Y. F. Han, J. W. Le, G. F. Huang, L. M. Lei, L. Xiao, and W. J. Lu: *Mater. Charact.* 2020, vol. 167. http://dx.doi.org/10.1016/j.matchar.2020.110458

46. Z. C. Sun, L. Liu, and H. Yang: *Mat Sci Eng a-Struct* 2011, vol. 528, pp. 5112-21. http://dx.doi.org/10.1016/j.msea.2011.03.039

47. Z. C. Sun, X. J. Mao, H. L. Wu, H. Yang, and J. J. Li: *Mat Sci Eng a-Struct* 2016, vol. 654, pp. 113-23. http://dx.doi.org/10.1016/j.msea.2015.12.031

48. S. Zhang, Y. Zhang, J. Qi, Z. Zou, and Y. Qian: *Materials* 2022, vol. 16. http://dx.doi.org/10.3390/ma16010160

49. A. D. Boccardo, Z. Zou, M. Simonelli, M. Tong, J. Segurado, S. B. Leen, and D. Tourret: *Materials & Design* 2024, vol. 241. http://dx.doi.org/10.1016/j.matdes.2024.112949

50. Yi Liu, Jianwen Liu, Hongfei Zhang, Yi Yang, Yuman Zhu, Aijun Huang, and Kai Zhang: *Materials Science and Engineering: A* 2025, vol. 937. http://dx.doi.org/10.1016/j.msea.2025.148449

51. Junjie Jiang, Zhihao Ren, Zhibo Ma, Tao Zhang, Peng Zhang, David Z. Zhang, and Zhongfa Mao: *Materials Science and Engineering: A* 2020, vol. 772. http://dx.doi.org/10.1016/j.msea.2019.138742

52. D. Banerjee and J. C. Williams: *Acta Mater.* 2013, vol. 61, pp. 844-79. http://dx.doi.org/10.1016/j.actamat.2012.10.043

53. I. Arganda-Carreras, V. Kaynig, C. Rueden, K. W. Eliceiri, J. Schindelin, A. Cardona, and H. Sebastian Seung: *Bioinformatics* 2017, vol. 33, pp. 2424-26. http://dx.doi.org/10.1093/bioinformatics/btx180

54. A. Fitzner, D. G. L. Prakash, J. Q. da Fonseca, M. Thomas, S. Y. Zhang, J. Kelleher, P. Manuel, and M. Preuss: *Acta Mater.* 2016, vol. 103, pp. 341-51. http://dx.doi.org/10.1016/j.actamat.2015.09.048

55. Zhiyi Zou Huseyin Hizli, James Murray, Adam Clare, Marco Simonelli: *J. Alloys Compd.* 2024, vol. 981, p. 173762. http://dx.doi.org/10.1016/j.jallcom.2024.173762

56. D. Hill, R. Banerjee, D. Huber, J. Tiley, and H. L. Fraser: *Scr. Mater.* 2005, vol. 52, pp. 387-92. http://dx.doi.org/10.1016/j.scriptamat.2004.10.019

57. Qi An, Lujun Huang, Qi Qian, Yong Jiang, Shuai Wang, Rui Zhang, Lin Geng, and Liqin Wang: *Journal of Materials Science & Technology* 2022, vol. 119, pp. 156-66. http://dx.doi.org/10.1016/j.jmst.2021.12.035
58. J. Le, C. J. Boehlert, G. F. Huang, J. W. Mao, L. M. Lei, Y. F. Han, and W. J. Lu: *Scr. Mater.* 2022, vol. 217, p. 114772. http://dx.doi.org/10.1016/j.scriptamat.2022.114772
59. I. Sen, R. S. Kottada, and U. Ramamurty: *Mat Sci Eng a-Struct* 2010, vol. 527, pp. 6157-65. http://dx.doi.org/10.1016/j.msea.2010.06.044
60. G. Singh, D. V. V. Satyanarayana, R. Pederson, R. Datta, and U. Ramamurty: *Mat Sci Eng a-Struct* 2014, vol. 597, pp. 194-203. http://dx.doi.org/10.1016/j.msea.2013.12.078
61. X. Chen, L. J. Huang, J. P. Song, S. P. Zhou, S. Wang, R. Zhang, and L. Geng: *Compos Part B-Eng* 2024, vol. 283. http://dx.doi.org/10.1016/j.compositesb.2024.111651
62. B. Cherukuri, R. Srinivasan, S. Tamirisakandala, and D. Miracle: *Scr. Mater.* 2009, vol. 60, pp. 496-99. http://dx.doi.org/10.1016/j.scriptamat.2008.11.040
63. S. Tamirisakandala, R. B. Bhat, J. S. Tiley, and D. B. Miracle: *Scr. Mater.* 2005, vol. 53, pp. 1421-26. http://dx.doi.org/10.1016/j.scriptamat.2005.08.020
64. S. S. Youssef, X. D. Zheng, S. S. Huang, Y. J. Ma, M. Qi, S. J. Zheng, J. F. Lei, and R. Yang: *J. Alloys Compd.* 2021, vol. 871. http://dx.doi.org/10.1016/j.jallcom.2021.159577
65. A. Venkataraman, P. A. Shade, R. Adebisi, S. Sathish, A. L. Pilchak, G. B. Viswanathan, M. C. Brandes, M. J. Mills, and M. D. Sangid: *Metall. Mater. Trans. A-Phys. Metall. Mater. Sci.* 2017, vol. 48a, pp. 2222-36. http://dx.doi.org/10.1007/s11661-017-4024-y
66. W. Xu, M. Brandt, S. Sun, J. Elambasseril, Q. Liu, K. Latham, K. Xia, and M. Qian: *Acta Mater.* 2015, vol. 85, pp. 74-84. http://dx.doi.org/10.1016/j.actamat.2014.11.028
67. P. Kumar and U. Ramamurty: *Acta Mater.* 2019, vol. 169, pp. 45-59. http://dx.doi.org/10.1016/j.actamat.2019.03.003
68. S. Tamirisakandala and D. B. Miracle: *International Journal of Advances in Engineering Sciences and Applied Mathematics* 2012, vol. 2, pp. 168-80. http://dx.doi.org/10.1007/s12572-011-0033-z
69. I. Sen, L. Maheshwari, S. Tamirisakandala, D. B. Miracle, and U. Ramamurty: *Mater. Sci. Eng. A* 2009, vol. 518, pp. 162-66. http://dx.doi.org/10.1016/j.msea.2009.04.039
70. C. S. Kim, I. Sohn, M. Nezafati, J. B. Ferguson, B. F. Schultz, Z. Bajestani-Gohari, P. K. Rohatgi, and K. Cho: *J. Mater. Sci.* 2013, vol. 48, pp. 4191-204. http://dx.doi.org/10.1007/s10853-013-7232-x
71. X. P. Li, G. Ji, Z. Chen, A. Addad, Y. Wu, H. W. Wang, J. Vleugels, J. Van Humbeeck, and J. P. Kruth: *Acta Mater.* 2017, vol. 129, pp. 183-93. http://dx.doi.org/10.1016/j.actamat.2017.02.062
72. Y. Q. Feng, K. Feng, C. W. Yao, Z. G. Li, and J. H. Sun: *Materials & Design* 2018, vol. 157, pp. 258-72. http://dx.doi.org/10.1016/j.matdes.2018.07.045
73. C. A. Schuh, T. G. Nieh, and H. Iwasaki: *Acta Mater.* 2003, vol. 51, pp. 431-43. http://dx.doi.org/10.1016/S1359-6454(02)00427-5
74. J. L. Murray, P. K. Liao, and K. E. Spear: *Bulletin of Alloy Phase Diagrams* 1986, vol. 7, pp. 550-55. http://dx.doi.org/10.1007/bf02869864
75. B. Guan, Y. C. Xin, X. X. Huang, C. L. Liu, P. D. Wu, and Q. Liu: *International Journal of*

Plasticity 2022, vol. 153, p. 103276. http://dx.doi.org/10.1016/j.ijplas.2022.103276

76. Jiyun Kang, Hyun Seok Oh, Shaolou Wei, Gaoming Zhu, Ikuho Nakahata, and Cemal Cem Tasan: *Acta Mater.* 2023, vol. 242. http://dx.doi.org/10.1016/j.actamat.2022.118424

77. Shaolou Wei, Jinwoo Kim, and Cemal Cem Tasan: *International Journal of Plasticity* 2022, vol. 148. http://dx.doi.org/10.1016/j.ijplas.2021.103131

78. P. Kumar, O. Prakash, and U. Ramamurty: *Acta Mater.* 2018, vol. 154, pp. 246-60. http://dx.doi.org/10.1016/j.actamat.2018.05.044

79. Hossein Beladi, Qi Chao, and Gregory S. Rohrer: *Acta Mater.* 2014, vol. 80, pp. 478-89. http://dx.doi.org/10.1016/j.actamat.2014.06.064

80. C. Goh, J. Wei, L. Lee, and M. Gupta: *Acta Mater.* 2007, vol. 55, pp. 5115-21. http://dx.doi.org/10.1016/j.actamat.2007.05.032

81. G. Liu, G. J. Zhang, F. Jiang, X. D. Ding, Y. J. Sun, J. Sun, and E. Ma: *Nat. Mater.* 2013, vol. 12, pp. 344-50. http://dx.doi.org/10.1038/nmat3544

82. Z. Zhang and D. L. Chen: *Scr. Mater.* 2006, vol. 54, pp. 1321-26. http://dx.doi.org/10.1016/j.scriptamat.2005.12.017

83. Dieter George Ellwood and David Bacon: *Mechanical Metallurgy*. third ed. McGraw-hill, New York, 1986.

84. H. J. Ryu, S. I. Cha, and S. H. Hong: *J. Mater. Res.* 2003, vol. 18, pp. 2851-58. http://dx.doi.org/10.1557/Jmr.2003.0398

85. L. J. Huang, L. Geng, H. X. Peng, and J. Zhang: *Scr. Mater.* 2011, vol. 64, pp. 844-47. http://dx.doi.org/10.1016/j.scriptamat.2011.01.011

86. Yakai Zhao, Kwang Boon Lau, Wei Hock Teh, Jing Jun Lee, Fengxia Wei, Ming Lin, Pei Wang, Cheng Cheh Tan, and Upadrasta Ramamurty: *J. Alloys Compd.* 2021, vol. 883, p. 160825. http://dx.doi.org/10.1016/j.jallcom.2021.160825

87. H. Zhang, J. Y. Zhang, J. P. Hou, D. D. Zhang, Y. H. Yue, G. Liu, and J. Sun: *Acta Mater.* 2022, vol. 241. http://dx.doi.org/10.1016/j.actamat.2022.118411

88. Peng-Cheng Zhao, Guang-Jian Yuan, Run-Zi Wang, Bo Guan, Yun-Fei Jia, Xian-Cheng Zhang, and Shan-Tung Tu: *Journal of Materials Science & Technology* 2021, vol. 83, pp. 196-207. http://dx.doi.org/10.1016/j.jmst.2021.01.019

89. G. H. Zhao, X. Z. Liang, B. Kim, and P. E. J. Rivera-Díaz-del-Castillo: *Materials Science and Engineering: A* 2019, vol. 756, pp. 156-60. http://dx.doi.org/10.1016/j.msea.2019.04.027

90. L. H. Dai, Z. Ling, and Y. L. Bai: *Compos Sci Technol* 2001, vol. 61, pp. 1057-63. http://dx.doi.org/10.1016/s0266-3538(00)00235-9

91. Lian Li, Panpan Ma, Ling Zhang, Hua Tan, and Miaoquan Li: *Composites Part B: Engineering* 2024, vol. 268. http://dx.doi.org/10.1016/j.compositesb.2023.111068

92. J. S. Zhang, X. H. Han, F. Chai, X. Hu, L. Hua, X. X. Fan, D. Y. Tian, and W. H. Zhuang: *J. Alloys Compd.* 2025, vol. 1036. http://dx.doi.org/10.1016/j.jallcom.2025.181955

93. M. H. Fang, Y. F. Han, Z. S. Shi, G. F. Huang, J. W. Song, and W. J. Lu: *Compos Part B-Eng* 2021, vol. 211, p. 108683. http://dx.doi.org/10.1016/j.compositesb.2021.108683

94. James C. Williams Gerd Lütjering: In *Engineering Materials, Processes*, Springer Berlin: Heidelberg, 2007.

95. Z. S. Ma, S. Wang, L. J. Huang, Q. An, R. Zhang, W. Q. Liu, F. B. Sun, R. Chen, and L. Geng:

Compos Part B-Eng 2023, vol. 254. http://dx.doi.org/10.1016/j.compositesb.2023.110583

96. T. Ahmed and H. J. Rack: *Mat Sci Eng a-Struct* 1998, vol. 243, pp. 206-11. http://dx.doi.org/10.1016/S0921-5093(97)00802-2